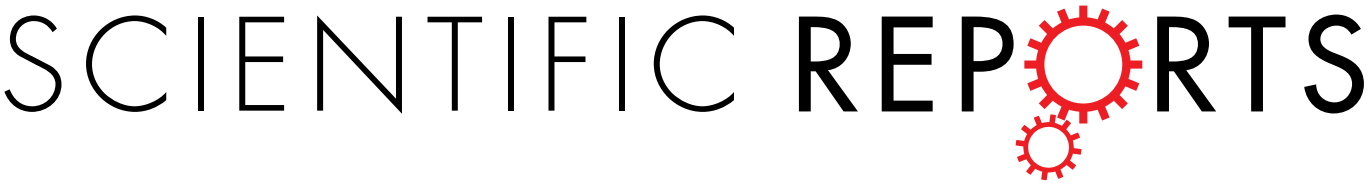

OPEN

Observation of low-loss broadband supermode propagation in coupled acoustic waveguide complex

Received: 19 January 2017
Accepted: 27 February 2017
Published: 28 March 2017

Ya-Xi Shen[1,*], Yu-Gui Peng[1,2,*], Xin-Cheng Chen[1], De-Gang Zhao[1] & Xue-Feng Zhu[1,2,3]

We investigate analytically, numerically, and experimentally the low-loss supermode propagation in a coupled acoustic waveguide complex within a broadband. The waveguide complex is implemented with air channels coupled via an ultrathin metafluid layer. We analytically derive the field distribution of incident sound needed for producing acoustic supermodes, and verify the periodically revival propagation in coupled waveguide systems numerically and experimentally. We find out that the supermode wavelength becomes longer for higher mode order or lower frequency. We have also demonstrated the robust propagation of supermodes in broadband. Our scheme can in principle be extended to three dimensions and the ultrasound regime with simplicity and may promote applications of high-fidelity signal transfer in complicated acoustic networks.

Anomalous manipulations of acoustic energy flow have received many attentions during the past decades, such as negative refraction/reflection[1–5], collimation[6–8], super-resolution imaging[9–11], cloaking[12–16], rainbow trapping[17–19], beam acceleration[20–22], and topological transportation[23–28], *etc*. The recent advances in acoustical metamaterials and metasurfaces provide a broad platform which enables those intriguing phenomena to be realized in experiments[29,30]. Due to diffraction, acoustic devices for anomalous wave-steering in free space are inevitably to be large in size. Therefore, a more promising candidate, *viz*. acoustic waveguide networks, is proposed for device integration, where the size may markedly decrease due to the lack of cut-off in rigid channels[10,11,25,27]. Previous works have shown that sound propagation in waveguide networks can be much more intricate than that in bulk media[25,27]. For example, the acoustic waves propagating in one waveguide may easily spread to the whole system through couplings. In practice, such coupling-induced diffraction is undesirable, since the information carried by acoustic signals will be smeared or considerably modified by diffraction during the propagation. It thus should be meaningful, both in physics and in engineering, to explore the possibility to realize non-diffracting acoustic wave propagation for high-fidelity signal transfer in integrated networks.

In this paper, we propose to employ supermodes to implement non-diffracting propagation in one type of acoustic networks, *viz.*, an array of coupled waveguides. The resulting device simply consists of five air channels coupled via four gratings. We rigorously derive the desired field distribution of incident waves for producing acoustic supermodes. Remarkably, the supermode propagations are featured with broadband stability and low loss, since the device has no resonant structures with frequency-dependent responses. We further demonstrate those intriguing properties of acoustic supermodes through proof-of-concept experiments. With the simple design and fabrication, our proposal can be in principle extended to three dimensions and the ultrasound regime, and make a significant step towards the application of high-fidelity transportation of broadband acoustic signals in integrated acoustic networks.

Results

We start from investigating the acoustic supermode in an array of N coupled waveguides based on the coupled-mode theory, with only the nearest-neighbor coupling being considered[31]. The scalar wave equation for sound takes the form of $\nabla^2 p - \frac{1}{c^2}\frac{\partial^2 p}{\partial t^2} = 0$. As shown in Fig. 1(a), we investigate a two-dimensional waveguide

[1]School of Physics, Huazhong University of Science and Technology, Wuhan, Hubei 430074, People's Republic of China. [2]Innovation Institute, Huazhong University of Science and Technology, Wuhan, Hubei 430074, People's Republic of China. [3]State Key Laboratory of Functional Materials for Informatics, Shanghai Institute of Microsystem and Information Technology, Chinese Academy of Sciences, 865 Changning Road, Shanghai 200050, People's Republic of China. *These authors contributed equally to this work. Correspondence and requests for materials should be addressed to X.-F.Z. (email: xfzhu@hust.edu.cn)

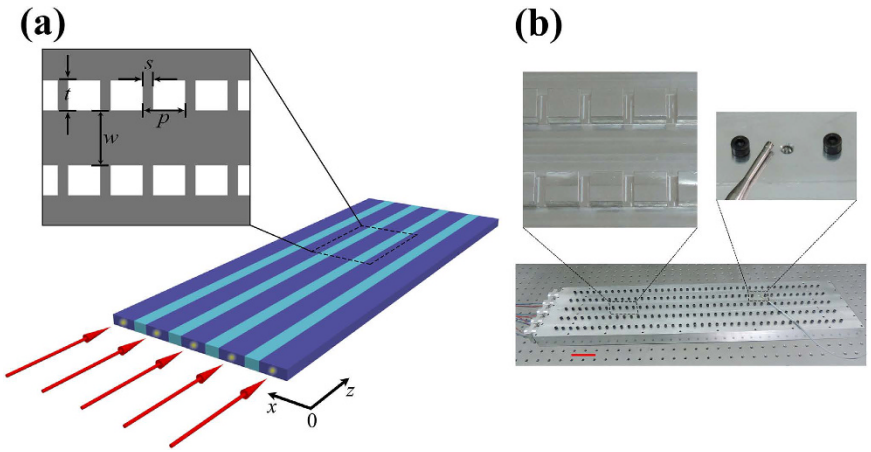

Figure 1. Schematic and Photograph of an acoustic waveguide array. (**a**) Schematic of the studied acoustic waveguide array, where five air channels are segregated by four gratings. The red arrows show the path of incident sound. Inset: Structure details of channels and gratings. The gray and white regions represent air and rigid metal, respectively. (**b**) Photograph of the fabricated acoustic waveguide array. Inset: machined inside channels, inside gratings, and measurement holes. Scale bar, 5 cm.

complex in x-z plane. Here, the pressure and speed of sound are expressed into $p = p(x, z)e^{i\omega t}$ and $c = \omega/k(x, z)$, where $k(x, z)$ represents the wave number. From the aforementioned equations, we can deduce the governing equation $\nabla^2 p + k(x, z)^2 p = 0$. For a linear and scalar system, we separate the variables to have $p(x, z) = p(x)p(z)$ and $k^2(x, z) = k_x^2 + \beta^2$, where β is the propagation constant along z direction. It should be pointed out that $\beta > k(x, y)$ for a guiding mode. Thus, k_x should be imaginary, indicating that the field along x direction is evanescent. Substituting $p(x, z) = p(x)p(z)$ and $k^2(x, z) = k_x^2 + \beta^2$ into the governing equation, we will obtain

$$\left\{\frac{\partial^2 p(x)}{\partial x^2} + k_x^2 p(x)\right\}p(z) + \left\{\frac{\partial^2 p(z)}{\partial z^2} + \beta^2 p(z)\right\}p(x) = 0, \tag{1}$$

which further leads to $\frac{\partial^2 p(z)}{\partial z^2} + \beta^2 p(z) = 0$ and $p(x, z) = F(x)e^{-i\beta z} + p_0$. Here, p_0 is a constant that could be chosen to be zero by setting a proper coordinate origin, and $F(x)$ is the mode profile along x direction. For an array of N coupled waveguides, $F(x)$ can be expressed into a discrete form of $F(x) = \sum_{l=1}^{N} A_l p_l$, with A_l being the weight of a propagating mode in one waveguide. Therefore, the mode profile of the whole system can be written into

$$p = \sum_{l=1}^{N} A_l p_l e^{-i\beta z}. \tag{2}$$

In this work, we only consider the nearest-neighbor coupling (the tight-binding model) and set all waveguides identical and equally spaced. Substituting Eq. (2) into the governing equation, we can finally derive the matrix

$$\begin{pmatrix} k_0^2 + \kappa_{11} & C & 0 & \cdots & 0 \\ C & k_0^2 + \kappa_{22} & C & \cdots & 0 \\ 0 & C & k_0^2 + \kappa_{33} & \cdots & 0 \\ \vdots & \vdots & \vdots & \ddots & \vdots \\ 0 & \cdots & 0 & C & k_0^2 + \kappa_{NN} \end{pmatrix} \begin{pmatrix} A_1 \\ A_2 \\ A_3 \\ \vdots \\ A_N \end{pmatrix} = \beta^2 \begin{pmatrix} A_1 \\ A_2 \\ A_3 \\ \vdots \\ A_N \end{pmatrix}, \tag{3}$$

where k_0 is the wave number in free space, C is the coupling coefficient between nearest neighbor waveguides, and $\kappa_{i,i}$ is the self-coupling coefficient for the ith waveguide. Due to different boundary conditions, the self-coupling coefficients κ_{11}, κ_{NN} do not equal to $\kappa_{i,i}(i = 2, 3, \ldots, N-1)$. Therefore, we may define $\kappa_a \equiv \kappa_{11}, \kappa_{NN}$, $\kappa_b \equiv \kappa_{22}, \kappa_{33}, \cdots \kappa_{N-1N-1}$, and $\delta\kappa = \kappa_b - \kappa_a$. After numerous mathematical deductions, the eigenvalues and eigenvectors of Eq. (3) are derived to be ref. 32

$$\begin{aligned} \beta_m &= \sqrt{k_0^2 + \kappa_b + 2C\ \cos\ \frac{m\pi}{N+1} + \mathrm{O}(\delta\kappa)}, \\ A_l^m &= \sqrt{\frac{2}{N+1}}\ \sin\ \frac{ml\pi}{N+1} + \mathrm{O}(\delta\kappa), \end{aligned} \tag{4}$$

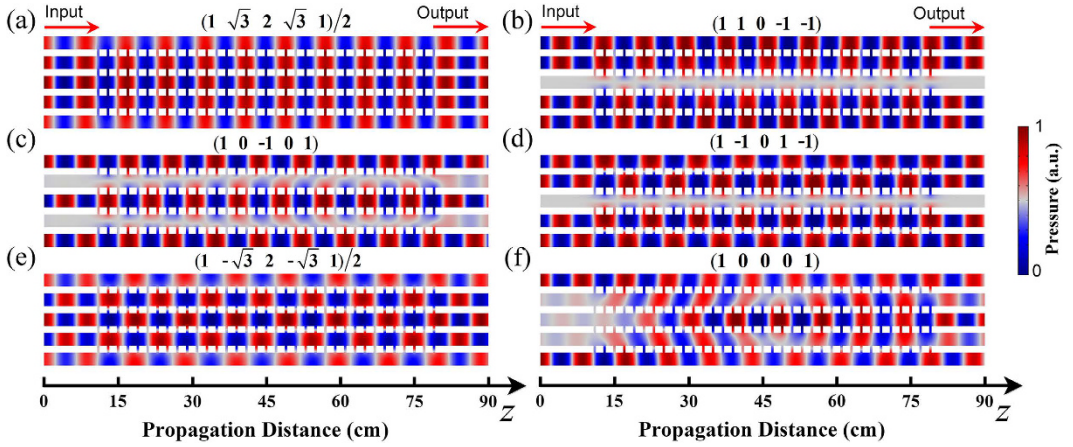

Figure 2. Pressure fields of different propagating modes. (**a–e**) Normalized pressure field distributions of five different supermodes at $m = 1, 2, 3, 4, 5$, respectively. The weight factors of all air channels for each supermode are appended on top of the corresponding panels. (**f**) Normalized pressure field distribution when the input does not form a supermode. The operation frequency $f = 4$ kHz.

where m is the mode order, and l is the waveguide number. In Eq. (4), β_m also represents the propagation constant of m-ordered supermode. It is interesting that the mode intensity in an air channel will be zero on condition that $ml/(N+1)$ is an integer, and the mode intensity will be non-zero for all air channels if $N+1$ is a prime number. From the above analysis, we derive that acoustic supermodes are actually the eigen-modes of the waveguide complex.

In this paper, the studied waveguide complex comprises five air channels segregated by four gratings ($N = 5$), as illustrated in Fig. 1(a,b). In our design, the channels and gratings are fabricated with Aluminum alloy that is treated as rigid to air. Propagating inside the waveguide complex, acoustic waves in one channel will be allowed to tunnel into the neighboring ones through periodic gratings. Based on the effective medium approach, acoustic gratings can be equivalent to metafluid layers with non-dispersive bulk modulus and density tensor in the long wave condition[10,11]. In respect that there are no local resonances as well as weak damping in air channels and metafluid layers, the wave propagation in this coupled waveguide array is featured with low energy loss in broadband. For the structural parameters, the thickness, slit width, and slit period of gratings are $t = 1.4$ cm, $s = 0.5$ cm, and $p = 2$ cm, respectively. The width of air channels $w = 2.6$ cm. According to Eq. (4), we can predict that there are five supermodes supported by the waveguide array since $N = 5$, and analytically obtain the weight factors of all air channels for each supermode by ignoring $\delta\kappa$.

Next, we simulate the sound propagation in an array of five coupled waveguides in Fig. 2(a–f), where the thermo-viscous damping effect is taken into consideration (see the Method section). In the numerical simulation, the total waveguide length is 90 cm. There are 35 slits connecting two adjacent channels. For convenience, we number the channels as 1, 2, 3, 4, 5 from below. Figure 2(a–e) show the normalized pressure field distributions for five different supermodes at $m = 1, 2, 3, 4, 5$, where the operation frequency $f = 4$ kHz and the excitation condition is determined by Eq. (4). The results clearly present the stable propagation of acoustic supermodes, where the field pattern is periodically repeated along z axis. We find out that the supermodes can be classified into symmetric and anti-symmetric ones for odd and even orders, respectively. To be specific, in Fig. 2(a,b), the supermode at $m = 1$ takes the form of $A^1 = (1/2,\ \sqrt{3}/2,\ 1,\ \sqrt{3}/2,\ 1/2)$, while the one at $m = 2$ is $A^2 = (1,\ 1,\ 0,\ -1,\ -1)$. From the field maps, we note that the waveguides at $(m, l, N) = (2, 3, 5)$, $(3, 2, 5)$, $(3, 4, 5)$, and $(4, 3, 5)$ are nearly "dark" due to destructive interferences, in well agreement with the aforementioned criterion that $ml/(N+1)$ should be an integer for $A_l^m = 0$. It should be pointed out that the acoustic supermode can be easily excited in experiments, since there are only two types of coupling between adjacent air channels, *viz.*, in-phase and out-of-phase couplings. Hence, we only need a simple voltage inverter circuit with tunable current amplitude and 0(or π)-phase to drive a set of emitters. By contrast, an arbitrarily chosen input (1, 0, 0, 0, 1) is sent into the coupled waveguide array. As shown in Fig. 2(f), after propagating through a certain distance, acoustic waves are clearly spreading to all channels via the coupling-induced diffraction, with pressure field pattern considerably modified at the output. In this case, the information carried by acoustic waves at the input can hardly be extracted at the output.

For characterizing wave propagations in the coupled waveguide array in details, we extract the waveforms of channels 1, 2, and 3 from the data in Fig. 2(a–f), as plotted by the curves in Fig. 3(a–f). Figure 3(a–e) show the waveforms of different supermodes from $z = 30$ cm to $z = 60$ cm at $m = 1, 2, 3, 4, 5$, respectively. For all the supermodes, sound in each air channel bears a stable propagation with the amplitude unchanged. As an example, for the supermode at $m = 1$ in Fig. 3(a), we clearly see the perfect sinusoidal waveforms in channels 1 (blue dot dash line), 2 (red dashed line), and 3 (black solid line), with the amplitude ratio being $1/2$: $\sqrt{3}/2$: 1 and phase locked. In the aforementioned theoretical part, we have shown that the supermode in a coupled waveguide array takes a modulated plane wave form of $p = \sum_{l=1}^{N} A_l p_l e^{-i\beta z}$. Therefore, it is predicted that the modal field will revive at intervals of $L_m = 2\pi/\beta_m$, *viz.*, supermode wavelength. From Eq. (4), β_m becomes smaller as m increases. We will obtain that the higher-ordered supermode has a longer wavelength. In Figure 3(a–e), the supermode wavelengths

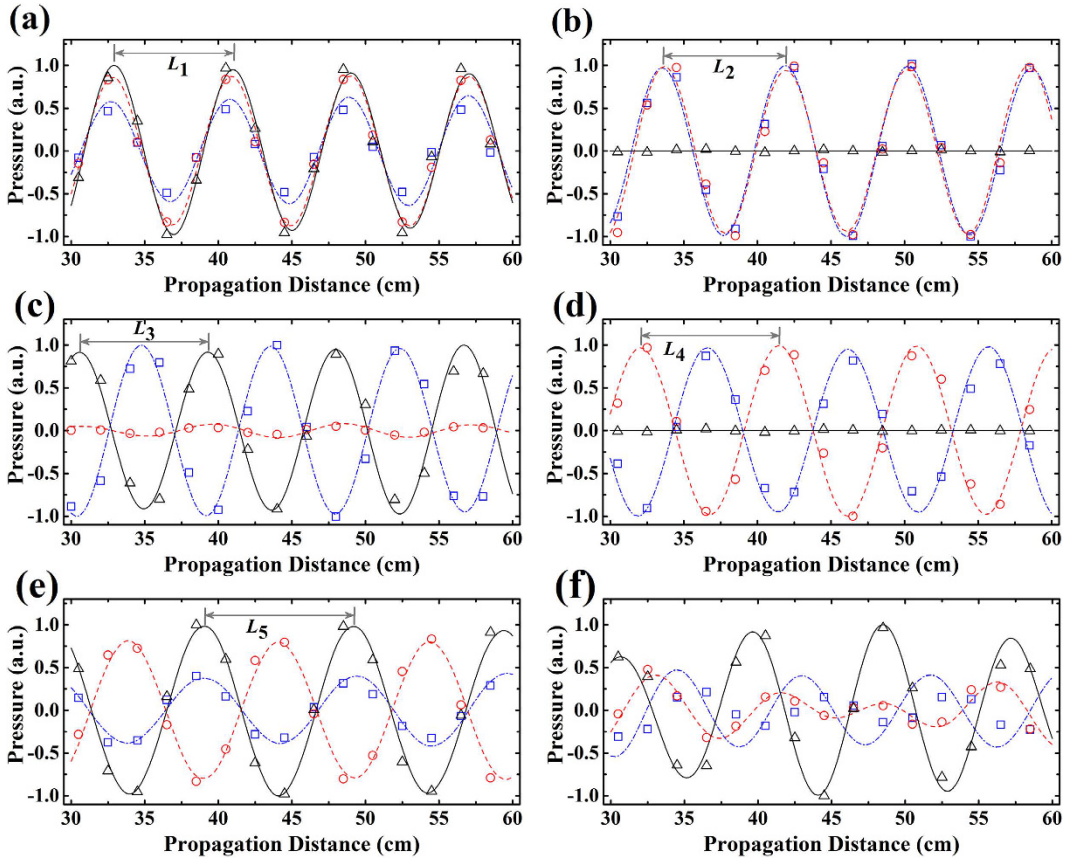

Figure 3. Numerical simulation and experimental measurement. (**a**–**f**) Simulated and measured pressure field distributions along the central line of channels 1, 2, and 3 from $z = 30$ cm to $z = 60$ cm, corresponding to the cases of Fig. 2(a–f), respectively. The blue dot dash line, red dashed line, and black solid line are the simulation data of channels 1, 2, and 3, while the blue squares, red circles, and black triangles are the measured data of channels 1, 2, and 3 in experiments. In (**a**–**e**), the wavelengths of five supermodes at $m = 1, 2, 3, 4, 5$, are marked by L_1, L_2, L_3, L_4, and L_5, respectively.

are numerically calculated to be $L_1 \approx 8.10$ cm, $L_2 \approx 8.36$ cm, $L_3 \approx 8.78$ cm, $L_4 \approx 9.54$ cm, and $L_5 \approx 10.33$ cm, which agrees well with the theoretical prediction. It should also be mentioned that we can further derive the coupling coefficient between nearest neighbor waveguides C and the self-coupling coefficient κ_b from the calculated supermode wavelengths L_m. In our case, we have $C \approx 7.67 \times 10^{-2}\,\mathrm{cm}^{-2}$ and $k_0^2 + \kappa_b \approx 0.513\,\mathrm{cm}^{-2}$. Figure 3(f) displays the waveform of a normal propagation mode in the coupled channels, featured with constantly changing wave amplitude and phase differences between two arbitrary channels.

To demonstrate the existence of acoustic supermodes experimentally, we have fabricated the sample of waveguide complex with five coupled air channels, and measured the pressure field through perforated holes, as shown in Fig. 1(b). For each air channel, there are 40 holes equally spaced by 2 cm. The details of experimental measurements are presented in the Method section. The measured results are shown by the dots in Fig. 3(a–f), where the blue squares, red circles, and black triangles are the measured data of channels 1, 2, and 3 after normalization. We clearly see that the experimental results are in very good agreement with numerical simulations.

We would also like to point out that the formation of acoustic supermode has nothing to do with frequency, as theoretically unveiled by Eq. (4). To verify this, we simulate the propagation of the 1st-ordered supermodes at two different frequencies of 4.5 kHz and 5 kHz, respectively, as shown in Fig. 4(a,b). The maps of pressure field distribution display the stable propagation of supermodes, in respect that the output signal is almost the same as the input. From the simulation, we can obtain the supermode wavelengths of the 1st-ordered supermodes at 4.5 kHz and 5 kHz, *viz.*, $L'_1 \approx 7.15$ cm and $L''_1 \approx 6.38$ cm, which shows that the supermode wavelength becomes longer at lower frequencies. In Figure 4(c,d), the experimental results agree with the simulation quite well, with both indicating that the designed waveguide complex can effectively support the acoustic supermode propagation in broadband.

At last, we show that our technique can be applied in the ultrasound regime, which might be useful in high-fidelity broadband underwater communication. In the proof-of-concept simulation, we employ Steel (mass density $\rho = 7.80 \times 10^3\,\mathrm{Kg/m}^3$; velocity of longitudinal waves $c_l = 6100$ m/s; velocity of transverse waves $c_t = 3300$ m/s) instead of Aluminum alloy to reduce solid-liquid coupling. The operation frequency is chosen to be 1.02 MHz. For the structural parameters scaled by approximately 0.022, the thickness, slit width, and

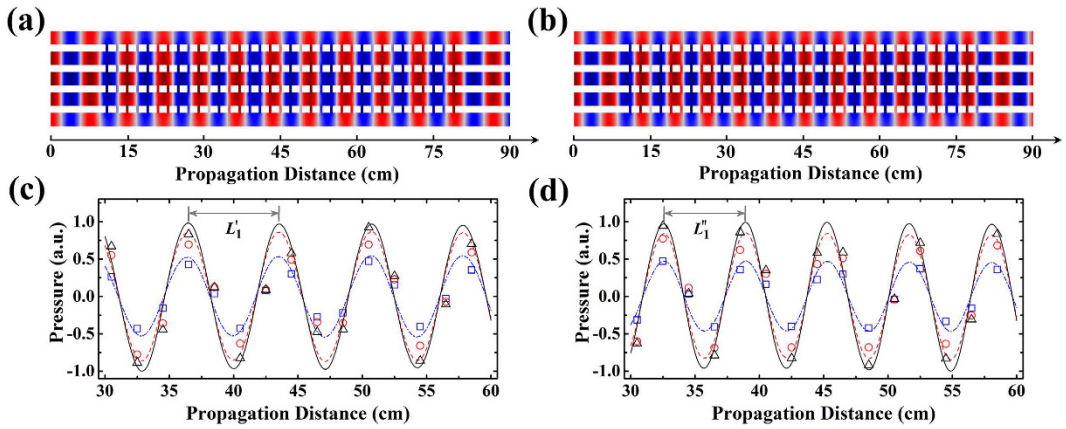

Figure 4. Robustness of acoustic supermodes at different frequencies. (**a**,**b**) Normalized pressure field distributions of the 1st-ordered supermodes at 4.5 kHz and 5 kHz, respectively. As predicted by Eq. (4), both supermodes take the same form of $A^1 = (1/2,\ \sqrt{3}/2,\ 1,\ \sqrt{3}/2,\ 1/2)$. (**c**,**d**) Simulated and measured pressure field distributions along the central line of channels 1, 2, and 3 from $z = 30$ cm to $z = 60$ cm, corresponding to the cases of (**a**) and (**b**), respectively. The blue dot dash line, red dashed line, and black solid line are the simulation data of channels 1, 2, and 3, while the blue squares, red circles, and black triangles are the measured data of channels 1, 2, and 3 in experiments.

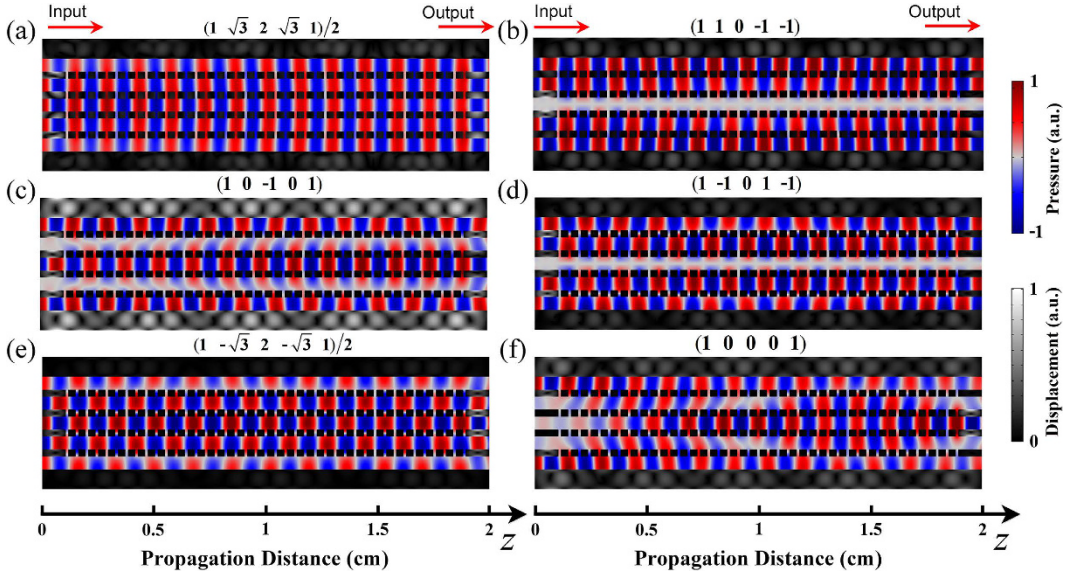

Figure 5. Pressure fields of different propagating modes in the ultrasound regime. (**a**–**e**) Normalized pressure field distributions of five different supermodes at $m = 1, 2, 3, 4, 5$, respectively. The weight factors of all water channels for each supermode are appended on top of the corresponding panels. (**f**) Normalized pressure field distribution when the input does not form a supermode. The operation frequency $f = 1.02$ MHz.

slit period of gratings are $t = 0.308$ mm, $s = 0.11$ mm, and $p = 0.44$ mm, respectively. The width of air channels $w = 0.572$ mm. We simulate the ultrasound propagation in the coupled waveguide complex in Fig. 5(a–f), where the thermo-viscous damping effect and solid-liquid coupling are taken into consideration. Even though there exist some field disturbances due to solid-liquid interaction, our results still reflect the characteristic propagation of acoustic supermodes, where the field pattern is periodically repeated along z axis.

Discussions

In summary, we have investigated the supermode propagation in coupled acoustic waveguides analytically, numerically, and experimentally. The experimental results agree well with the theoretical prediction and numerical simulation. The proposed device bears the advantages of easy fabrication, small fingerprint, low-loss and broadband performance, as well as the potential to further extend into higher dimensions and the ultrasound regime, which is very promising in various practical applications, such as underwater acoustic communication, ultrasound imaging, and sensing, *etc*. Our study may pave the way to explore other types of anomalous wave manipulation in integrated acoustic networks.

Methods

Numerical simulation. Throughout this paper, we consider the thermo-viscous damping in all numerical simulations by employing thermo-acoustics module of COMSOL Multiphysics™ 5.2. A perfectly matched layer is added at the right side to prevent reflections. In the ultrasound simulation, the solid-fluid interaction is also take into consideration.

Experimental measurement. In the experiment, we employ a multi-function waveform generator (RIGOL DG1032Z) and a stable power amplifier (AOSIBAO A8 HIFI) to output multiple locked sinusoidal electrical signals, and then use a connected full-range driver (HiVi B1S) to convert the electrical signals into sound. The pressure field is measured by a 1/8-inch diameter Brüel&Kjær Type-LAN-XI-3160 condenser microphone. All data are recorded and processed with Brüel&Kjær PULSE 3160-A-042 4-channel analyser. During the field measurement, other unmeasured holes are plugged with screws to prevent sound leakage.

References

1. Zhang, X. D. & Liu, Z. Y. Negative refraction of acoustic waves in two-dimensional phononic crystals. *Appl. Phys. Lett.* **85,** 341 (2004).
2. Ke, M. Z., Liu, Z. Y., Qiu, C. Y., Wang, W. G. & Shi, J. Negative-refraction imaging with two-dimensional phononic crystals. *Phys. Rev. B* **72,** 064306 (2005).
3. Feng, L. *et al.* Acoustic Backward-Wave Negative Refractions in the Second Band of a Sonic Crystal. *Phys. Rev. Lett.* **96,** 014301 (2006).
4. Kaina, N., Lemoult, F., Fink, M. & Lerosey, G. Negative refractive index and acoustic superlens from multiple scattering in single negative metamaterials. *Nature* **525,** 77 (2015).
5. Zhao, D. G., Ye, Y. T., Xu, S. J., Zhu, X. F. & Yi, L. Broadband and wide-angle negative reflection at a phononic crystal boundary. *Appl. Phys. Lett.* **104,** 043503 (2014).
6. Christensen, J., Fernandez-Dominguez, A. I., Leon-Perez, F. D., Martin-Moreno, L. & Garcia-Vida, F. J. Collimation of sound assisted by acoustic surface waves. *Nat. Phys.* **3,** 851 (2007).
7. He, Z. J. *et al.* Acoustic collimating beams by negative refraction in two-dimensional phononic crystal. *J. Appl. Phys.* **105,** 116105 (2009).
8. Shi, J. J., Lin, S. S. & Huang, T. J. Wide-band acoustic collimating by phononic crystal composites. *Appl. Phys. Lett.* **92,** 111901 (2008).
9. Jia, H. *et al.* Subwavelength imaging by a simple planar acoustic superlens. *Appl. Phys. Lett.* **97,** 173507 (2010).
10. Li, J., Fok, L., Yin, X. B., Bartal, G. & Zhang, X. Experimental demonstration of an acoustic magnifying hyperlens. *Nat. Mater.* **8,** 931 (2009).
11. Zhu, J. *et al.* A holey-structured metamaterial for acoustic deep-subwavelength imaging. *Nat. Phys.* **7,** 52 (2011).
12. Chen, H. Y. & Chan, C. T. Acoustic cloaking in three dimensions using acoustic metamaterials. *Appl. Phys. Lett.* **91,** 183518 (2007).
13. Zhang, S., Xia, C. G. & Fang, N. Broadband Acoustic Cloak for Ultrasound Waves. *Phys. Rev. Lett.* **106,** 024301 (2011).
14. Zhu, X. F., Liang, B., Kan, W. W., Zou, X. Y. & Cheng, J. C. Acoustic Cloaking by a Superlens with Single-Negative Materials. *Phys. Rev. Lett.* **106,** 014301 (2011).
15. Zhu, X. F., Ramezani, H., Shi, C. Z., Zhu, J. & Zhang, X. PT-Symmetric Acoustics. *Phys. Rev. X* **4,** 031042 (2014).
16. Li, Y., Liang, B., Gu, Z. M., Zou, X. Y. & Cheng, J. C. Unidirectional acoustic transmission through a prism with near-zero refractive index. *Appl. Phys. Lett.* **103,** 053505 (2013).
17. Zhu, J. *et al.* Acoustic rainbow trapping. *Sci. Rep.* **3,** 1728 (2013).
18. Jia, H., Lu, M. H., Ni, X., Bao, M. & Li, X. D. Spatial separation of spoof surface acoustic waves on the graded groove grating. *J. Appl. Phys.* **116,** 124504 (2014).
19. Chen, Y. Y., Liu, H. J., Reilly, M., Bae, H. & Yu, M. Enhanced acoustic sensing through wave compression and pressure amplification in anisotropic metamaterials. *Nat. Commun.* **5,** 5247 (2015).
20. Li, Y. *et al.* Experimental realization of full control of reflected waves with subwavelength acoustic metasurfaces. *Phys. Rev. Appl.* **2,** 064002 (2014).
21. Li, Y., Jiang, X., Liang, B., Cheng, J. C. & Zhang, L. K. Metascreen-based acoustic passive phased array. *Phys. Rev. Appl.* **4,** 024003 (2015).
22. Zhu, X. F. *et al.* Implementation of dispersion-free slow acoustic wave propagation and phase engineering with helical-structured metamaterials. *Nat. Commun.* **7,** 11731 (2016).
23. Yang, Z. J. *et al.* Topological acoustics. *Phys. Rev. Lett.* **114,** 114301 (2015).
24. Khanikaev, A. B., Fleury, R., Mousavi, S. H. & Alù, A. Topologically robust sound propagation in an angular-momentum-biased graphene-like resonator lattice. *Nat. Commun.* **6,** 8240 (2015).
25. Fleury, R., Khanikaev, A. B. & Alù, A. Floquet topological insulators for sound. *Nat. Commun.* **7,** 11744 (2016).
26. He, C. *et al.* Acoustic topological insulator and robust one-way sound transport. *Nat. Phys.* **12,** 1124 (2016).
27. Peng, Y. G. *et al.* Experimental demonstration of anomalous Floquet topological insulator for sound. *Nat. Commun.* **7,** 13368 (2016).
28. Lu, J. Y. *et al.* Observation of topological valley transport of sound in sonic crystals. *Nat. Phys.*, doi: 10.1038/NPHYS3999 (2016).
29. Ma, G. C. & Sheng, P. Acoustic metamaterials: From local resonances to broad horizons. *Sci. Adv.* **2,** e1501595 (2016).
30. Cummer, S. A., Christensen, J. & Alù, A. Controlling sound with acoustic metamaterials. *Nat. Rev. Mater.* **1,** 16001 (2016).
31. Hardy, A. & Streifer, W. Coupled-mode theory of parallel waveguides. *J. Lightwave Technol.* **LT-3,** 1135 (1985).
32. Cooper, M. L. & Mookherjea, S. Numerically-assisted coupled-mode theory for silicon waveguide couplers and arrayed waveguides. *Opt. Express* **17,** 1583 (2009).

Acknowledgements

This work was supported by National Natural Science Foundation of China (Grant Nos. 11674119, 11690030, 11690032, 11404125). X. F. Z. acknowledges the financial support from the Bird Nest Plan of HUST.

Author Contributions

Y.X.S. and Y.G.P. carried out the numerical simulations and theoretical analysis. Y.X.S. and X.C.C. fabricated the sample and did the experiments. X.F.Z., Y.X.S., D.G.Z. and Y.G.P. contributed in the discussion of theoretical analysis and wrote the paper. X.F.Z. conceived and supervised the study.

Additional Information

Competing Interests: The authors declare no competing financial interests.

How to cite this article: Shen, Y.-X. *et al.* Observation of low-loss broadband supermode propagation in coupled acoustic waveguide complex. *Sci. Rep.* **7**, 45603; doi: 10.1038/srep45603 (2017).

Publisher's note: Springer Nature remains neutral with regard to jurisdictional claims in published maps and institutional affiliations.

This work is licensed under a Creative Commons Attribution 4.0 International License. The images or other third party material in this article are included in the article's Creative Commons license, unless indicated otherwise in the credit line; if the material is not included under the Creative Commons license, users will need to obtain permission from the license holder to reproduce the material. To view a copy of this license, visit http://creativecommons.org/licenses/by/4.0/

© The Author(s) 2017